

Supporting Information for “Microseismic Constraints on the Mechanical State of the North Anatolian Fault Zone Thirteen Years after the 1999 M7.4 Izmit Earthquake”

Eric Beaucé^{1,3}, Robert D. van der Hilst¹, Michel Campillo^{2,1}

¹Department of Earth, Atmospheric, and Planetary Sciences, Massachusetts Institute of Technology, USA

²Institut des Sciences de la Terre, Université Grenoble Alpes, France

³Lamont-Doherty Earth Observatory, Columbia University, NY, USA

Contents of this file

1. Texts S1 to S2.
2. Table S1.
3. Figures S1 to S8.

Text S1: Earthquake Catalog

Text S1.1: Velocity Model

The P- and S-wave velocity model used for detecting and locating earthquakes is shown in Table S1.

Text S1.2: Automated Phase Picking with PhaseNet

The threshold on P- and S-wave probabilities to trigger a P- or S-wave pick with PhaseNet (Zhu & Beroza, 2019) is 0.6.

Text S1.3: Absolute Earthquake Location with NonLinLoc

NonLinLoc (NLLoc, Lomax et al., 2000, 2009) offers different loss functions to minimize to find the best earthquake location given a set of P- and S-wave arrival times. Beside the classic L2 norm of the residuals, NLLoc can maximize the equal differential time (abbreviated EDT in the software) likelihood function, which is robust to outliers. Since outliers often arise in a fully automated method, the choice of the EDT likelihood function is key for producing correct earthquake locations.

The maximum of the EDT likelihood function is searched with the oct-tree importance sampling algorithm, which combines random sampling and grid-search to speed up the grid-search method and use an adaptive grid that is finer in regions of higher likelihood. Our initial grid has 10 cells in longitude and latitude, and 6 cells in depth. We draw 5000 samples inside each cell and use the station density when deciding which grid cells to further subdivide. The initial grid has 1 km-spaced nodes in the horizontal directions and 0.5 km-spaced in the vertical direction.

Text S1.4: Double-difference Relative Relocation with GrowClust

GrowClust (Trugman & Shearer, 2017) is an earthquake relative relocation software based on the double-difference method. We compute the inter-event differential times on each station and component by cross-correlating the P-wave and S-wave first arrivals and search for the lag times that maximize the correlation coefficient (CC). P- and S-wave windows are 2 s long and start 0.4 s before the P and S wave, respectively, the sampling rate is 50 Hz, and waveforms are filtered between 2 Hz and 12 Hz.

All differential time observations with $CC > 0.60$ ($rmincut = 0.60$ in the control file), and an event pair is kept only if the average CC is greater than 0.33 ($rpsavgmin = 0.33$ in the control file) and at least 5 differential time observations have $CC > 0.50$ ($rmin = 0.50$ and $ngoodmin = 5$).

Text S1.5: Earthquake Catalog File

The earthquake catalog is a csv file with one row per event. The columns of the file are:

- origin_times: Origin times of the events.
- latitudes: Latitudes of the events, in decimal degrees.
- longitudes: Longitudes of the events, in decimal degrees.
- depths: Depths of the events, in km.
- max_hor_uncertainty: Maximum location uncertainty in the horizontal direction, in km.
- max_ver_uncertainty: Maximum location uncertainty in the vertical direction, in km.
- location_quality: 2 - good, 1 - intermediate, 0 - bad (do not trust it).
- magnitudes: Local magnitudes of the events. -10 if no estimate is available.
- fractal_dimensions: Fractal dimension of the earthquake occurrence time series of the template the event was detected with.
- tids: Template ID of the template that detected the event.
- mining_activity: True if the event was detected with a mining related template, False otherwise.

Text S1.6: Magnitude Estimation

Within each family of earthquakes detected by a same template, we computed the S-wave spectra with the multi-taper method (Prieto et al., 2009). The SNR was computed in the spectral domain as the ratio of the S-wave spectrum to the spectrum of a noise window taken before the P wave. The SNR was used to compute the multi-channel weighted average of the S-wave spectra (see Equation (1) and Figure S1A).

$$\bar{v}(f) = \frac{1}{W(f)} \sum_{s,c} w_{s,c} \alpha_{s,c} v_{s,c}(f), \quad W(f) = \sum_{s,c} w_{s,c}(f). \quad (1)$$

In Equation (1), $v_{s,c}(f)$ is the velocity spectrum of station s , component c at frequency f , $w_{s,c}$ is the corresponding weight (see Figure S1A) and $\alpha_{s,c}$ is the factor that corrects for geometric spreading and attenuation (see Equation (5)). The average spectra were converted to displacement spectra $u(f)$ and fitted with the Brune model (Equation (2), Brune, 1970):

$$|u_{\text{Brune}}(f)| = \frac{\Omega_0}{\left(1 + \frac{f}{f_c}\right)^2}, \quad (2)$$

where Ω_0 is the low-frequency plateau, which is proportional to the seismic moment M_0 , and f_c is the corner frequency. The successfully fitted spectra gave a seismic moment estimate using Equation (3) (Richards, 1971).

$$|u^S(f)| = \frac{R^S}{2\rho\beta^3r} \frac{M_0}{1 + \left(\frac{f}{f_c}\right)^2} \exp\left(-\frac{\pi ft_{s,c}^S}{Q^S(f)}\right), \quad (3)$$

$$\implies M_0 = \frac{\Omega_0 2\rho\beta^3r}{R^S} \exp\left(\frac{\pi ft_{s,c}^S}{Q^S(f)}\right), \quad (4)$$

$$\implies \alpha_{s,c} = \frac{2\rho\beta^3r_{s,c}}{R^S} \exp\left(\frac{\pi ft_{s,c}^S}{Q^S(f)}\right). \quad (5)$$

In Equation (3-5), we used typical values for the S-wave velocity β (3000 km/s), the density of crustal rocks ρ (2700 kg/m³) and the average S-wave radiation pattern R^S

($\sqrt{2/5}$ from Aki & Richards, 2002). The source-receiver distance $r_{s,c}$ and the S-wave travel time $t_{s,c}^S$ were computed from the source location and velocity model. Finally, a frequency dependent quality factor was obtained from Izgi, Eken, Gaebler, Eulenfeld, and Taymaz (2020). The moment magnitude M_w is:

$$M_w = \frac{2}{3} (\log M_0 - 9.1). \quad (6)$$

Once moment magnitude estimates $M_w = M_{\text{ref}}$ were available for at least one event in a template family, we estimated a local magnitude $M_{L,i}$ for all other events i based on log amplitude ratios:

$$M_{L,i} = M_{\text{ref}} + \text{Median}_{s,c} \left\{ \log \frac{A_{s,c}^i}{A_{s,c}^{\text{ref}}} \right\}, \quad (7)$$

or more generally if there are several reference events:

$$M_{L,i} = \text{Median}_k \left\{ M_{\text{ref},k} + \text{Median}_{s,c} \left\{ \log \frac{A_{s,c}^i}{A_{s,c}^{\text{ref},k}} \right\} \right\}. \quad (8)$$

Using Equation (8) to compute a local magnitude M_L for every event with a moment magnitude M_w , we measured the scaling between M_w and M_L and built the calibration first-order relationship $M_w = A + BM_L$ (see Figure S1B).

Text S1.7: Gutenberg-Richter b-value

The frequency-magnitude distribution of earthquakes typically follows the Gutenberg-Richter law (Gutenberg & Richter, 1941):

$$\log N(M) = a - bM. \quad (9)$$

In Equation (9), $N(M)$ is the number of earthquakes with magnitude greater than M , the a-value depends on the total number of observed events, and the b-value controls

how frequent larger earthquakes are (typically $b \approx 1$). We estimated the b-value with the maximum likelihood technique (Aki, 1965):

$$b = \frac{1}{\ln(10) (\bar{M} - M_c)}. \quad (10)$$

Equation (10) is derived for continuous magnitudes M (no bias from binned magnitudes). M_c is the magnitude of completeness, *i.e.* the magnitude above which all events are detected. We computed M_c with the maximum curvature technique (*e.g.* Wiemer & Katsumata, 1999), that is, taking the mode of the (non-cumulative) frequency-magnitude distribution as the magnitude of completeness. We used the kernel density method to estimate the probability density function (pdf) of the frequency-magnitude distribution. We computed M_c on the pdf instead of the raw histogram to mitigate the bin-size dependence of the M_c estimate. The estimation of b-value and magnitude of completeness is illustrated on two earthquake populations in Figure S2.

At each template location, we selected all the templates within a 5 km-radius and used the events they detected to compute b and M_c . Following Tormann, Wiemer, Metzger, Michael, and Hardebeck (2013), we imposed a minimum of 50 events to compute the b-value and, in addition, requested a minimum of 30 events above the magnitude of completeness. As these numbers are still low, we carefully estimated the uncertainties to assess the statistical significance of b-value differences between different groups following Utsu (1966). The confidence interval for a single b-value can be derived from its probability density function ρ :

$$\rho(\hat{b}) = \frac{n^n}{\Gamma(n)} \left(\frac{b}{\hat{b}}\right)^{n+1} e^{-n\frac{b}{\hat{b}}\frac{1}{b}}, \quad (11)$$

where \hat{b} is the b-value random variable, b is the estimate as given by Equation (10), n is the number of earthquakes with magnitude $M > M_c$, and Γ is the gamma function. Confidence intervals were derived from the percentiles of the cumulative distribution function (see Figure S2C).

Utsu (1966) also noted that the b-value ratio between two populations 1 and 2 follows the F distribution with degrees of freedom $2n_1$ and $2n_2$, where n_1 and n_2 are the numbers of earthquakes with $M > M_c$ in groups 1 and 2, respectively:

$$\frac{\hat{b}_2 b_1}{\hat{b}_1 b_2} \sim F(2n_1, 2n_2). \quad (12)$$

In Equation (12), the groups are indexed such that $b_1 > b_2$. The confidence level at which the two b-values are different is equal to the probability that $\hat{b}_1 > \hat{b}_2$:

$$\mathbb{P}(\hat{b}_1 > \hat{b}_2) = \mathbb{P}\left(\frac{\hat{b}_2 b_1}{\hat{b}_1 b_2} < \frac{b_1}{b_2}\right) \equiv \text{cdf}_{F(2n_1, 2n_2)}\left(\frac{b_1}{b_2}\right). \quad (13)$$

In Equation (13), the right-hand term is the cumulative distribution function (cdf) of the F distribution. This method is exemplified at Figure S2D.

Text S1.8: Identifying Mining Templates

Mining seismicity is identified by looking at the statistics of the detected events' time of the day within each family of events detected with a same template. See Figure S3. We compared the locations of mining-related seismicity identified by our analysis with the explosions (quarry blasts) reported in the Kandilli catalog (see Figure S4).

Text S1.9: Comparison with the Frequency-Magnitude Distribution of the Poyraz et al. 2015 Catalog

Comparison of the frequency-magnitude distributions of the hand-made catalog in Poyraz et al. (2015) and our catalog. See Figure S5.

Text S1.10: Comparison with the Frequency-Magnitude Distributions of the Past Seismicity

Comparison of the frequency-magnitude distributions of the pre-, co-, and post-Izmit seismicity with the 2012-2013 seismicity. See Figure S6.

Text S2: Temporal Clustering

Extra information on temporal clustering:

- Extended temporal clustering analysis, see Figure S7.
- A transient increase in the Poisson rate of a Poisson point process does not produce temporal clustering (see Figure S8). The increase itself may have a power-law time dependence, but we argue that, in this case, it must be caused by an interaction-driven mechanism.

References

- Aki, K. (1965). Maximum likelihood estimate of b in the formula $\log n = a - bm$ and its confidence limits. *Bull. Earthq. Res. Inst., Tokyo Univ.*, 43, 237–239.
- Aki, K., & Richards, P. G. (2002). *Quantitative seismology*.
- Bohnhoff, M., Ickrath, M., & Dresen, G. (2016). Seismicity distribution in conjunction with spatiotemporal variations of coseismic slip and postseismic creep along the combined 1999 izmit-düzce rupture. *Tectonophysics*, 686, 132–145.

- Brune, J. N. (1970). Tectonic stress and the spectra of seismic shear waves from earthquakes. *Journal of geophysical research*, 75(26), 4997–5009.
- Bulut, F., Bohnhoff, M., Aktar, M., & Dresen, G. (2007). Characterization of aftershock-fault plane orientations of the 1999 İzmit (turkey) earthquake using high-resolution aftershock locations. *Geophysical Research Letters*, 34(20).
- Gutenberg, B., & Richter, C. (1941). *Seismicity of the earth* (Vol. 34). Geological Society of America.
- Ickrath, M., Bohnhoff, M., Dresen, G., Martinez-Garzon, P., Bulut, F., Kwiatek, G., & Germer, O. (2015). Detailed analysis of spatiotemporal variations of the stress field orientation along the izmit-düzce rupture in nw turkey from inversion of first-motion polarity data. *Geophysical Journal International*, 202(3), 2120–2132.
- Izgi, G., Eken, T., Gaebler, P., Eulenfeld, T., & Taymaz, T. (2020). Crustal seismic attenuation parameters in the western region of the north anatolian fault zone. *Journal of Geodynamics*, 134, 101694.
- Karabulut, H., Schmittbuhl, J., Özalaybey, S., Lengline, O., Kömeç-Mutlu, A., Durand, V., ... Bouin, M. (2011). Evolution of the seismicity in the eastern Marmara Sea a decade before and after the 17 August 1999 İzmit earthquake. *Tectonophysics*, 510(1-2), 17–27.
- Lomax, A., Michelini, A., Curtis, A., & Meyers, R. (2009). Earthquake location, direct, global-search methods. *Encyclopedia of complexity and systems science*, 5, 2449–2473.
- Lomax, A., Virieux, J., Volant, P., & Berge-Thierry, C. (2000). Probabilistic earthquake location in 3D and layered models. In *Advances in seismic event location* (pp. 101–

134). Springer.

Poyraz, S. A., Teoman, M. U., Türkelli, N., Kahraman, M., Cambaz, D., Mutlu, A., ... others (2015). New constraints on micro-seismicity and stress state in the western part of the North Anatolian Fault Zone: Observations from a dense seismic array. *Tectonophysics*, *656*, 190–201.

Prieto, G. A., Parker, R., & Vernon Iii, F. (2009). A fortran 90 library for multitaper spectrum analysis. *Computers & Geosciences*, *35*(8), 1701–1710.

Richards, P. G. (1971). An elasticity theorem for heterogeneous media, with an example of body wave dispersion in the earth. *Geophysical Journal International*, *22*(5), 453–472.

Tormann, T., Wiemer, S., Metzger, S., Michael, A., & Hardebeck, J. L. (2013). Size distribution of parkfield's microearthquakes reflects changes in surface creep rate. *Geophysical Journal International*, *193*(3), 1474–1478.

Trugman, D. T., & Shearer, P. M. (2017). GrowClust: A hierarchical clustering algorithm for relative earthquake relocation, with application to the Spanish Springs and Sheldon, Nevada, earthquake sequences. *Seismological Research Letters*, *88*(2A), 379–391.

Utsu, T. (1966). A statistical significance test of the difference in b-value between two earthquake groups. *Journal of Physics of the Earth*, *14*(2), 37–40.

Wiemer, S., & Katsumata, K. (1999). Spatial variability of seismicity parameters in after-shock zones. *Journal of Geophysical Research: Solid Earth*, *104*(B6), 13135–13151.

Zhu, W., & Beroza, G. C. (2019). PhaseNet: a deep-neural-network-based seismic arrival-time picking method. *Geophysical Journal International*, *216*(1), 261–273.

| Depth (top of the layer, km) | v_P (km/s) | v_S (km/s) |
|------------------------------|--------------|--------------|
| -2 | 2.900 | 1.670 |
| 0 | 3.000 | 1.900 |
| 1 | 5.600 | 3.150 |
| 2 | 5.700 | 3.210 |
| 3 | 5.800 | 3.260 |
| 4 | 5.900 | 3.410 |
| 5 | 5.950 | 3.420 |
| 6 | 6.050 | 3.440 |
| 8 | 6.100 | 3.480 |
| 10 | 6.150 | 3.560 |
| 12 | 6.200 | 3.590 |
| 14 | 6.250 | 3.610 |
| 15 | 6.300 | 3.630 |
| 20 | 6.400 | 3.660 |
| 22 | 6.500 | 3.780 |
| 25 | 6.700 | 3.850 |
| 32 | 8.000 | 4.650 |
| 77 | 8.045 | 4.650 |

Table S1. 1D velocity model due to Karabulut et al. (2011) used in this study.

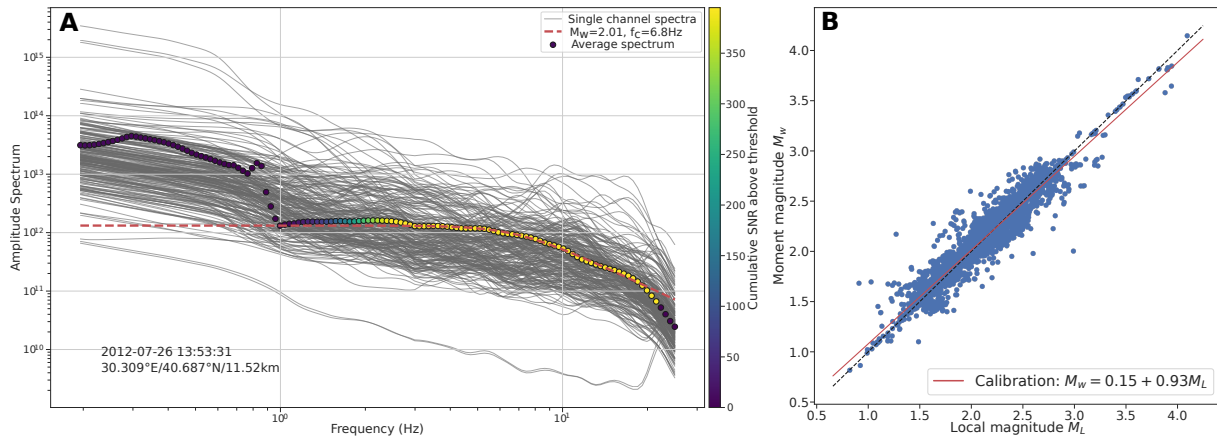


Figure S1. A: Average S-wave spectrum fitted with the Brune model (red curve). This is a weighted average of all single-channel S-wave spectra (thin grey spectra, Equation (1) of the supplementary material). The weight of each frequency bin of each channel is proportional to the excess signal-to-noise ratio (SNR) defined as $w(f) = \text{SNR}(f) - \text{SNR}_t(f)$, where $\text{SNR}_t(f)$ is the minimum SNR value that the frequency bin f must exceed in order to contribute to the average. Every frequency bin of the average spectrum also has a weight that is equal to the sum of the single-channel weights. Note that because we correct the single-channel spectra for geometric spreading and attenuation, the low-frequency plateau shown here gives directly the seismic moment M_0 . **B:** Scaling between moment magnitude M_w and local magnitude M_L . All events with a moment magnitude estimate also have a local magnitude computed with Equation (??) in the main text. The calibration is close to identity: $M_w = 0.15 + 0.93M_L$.

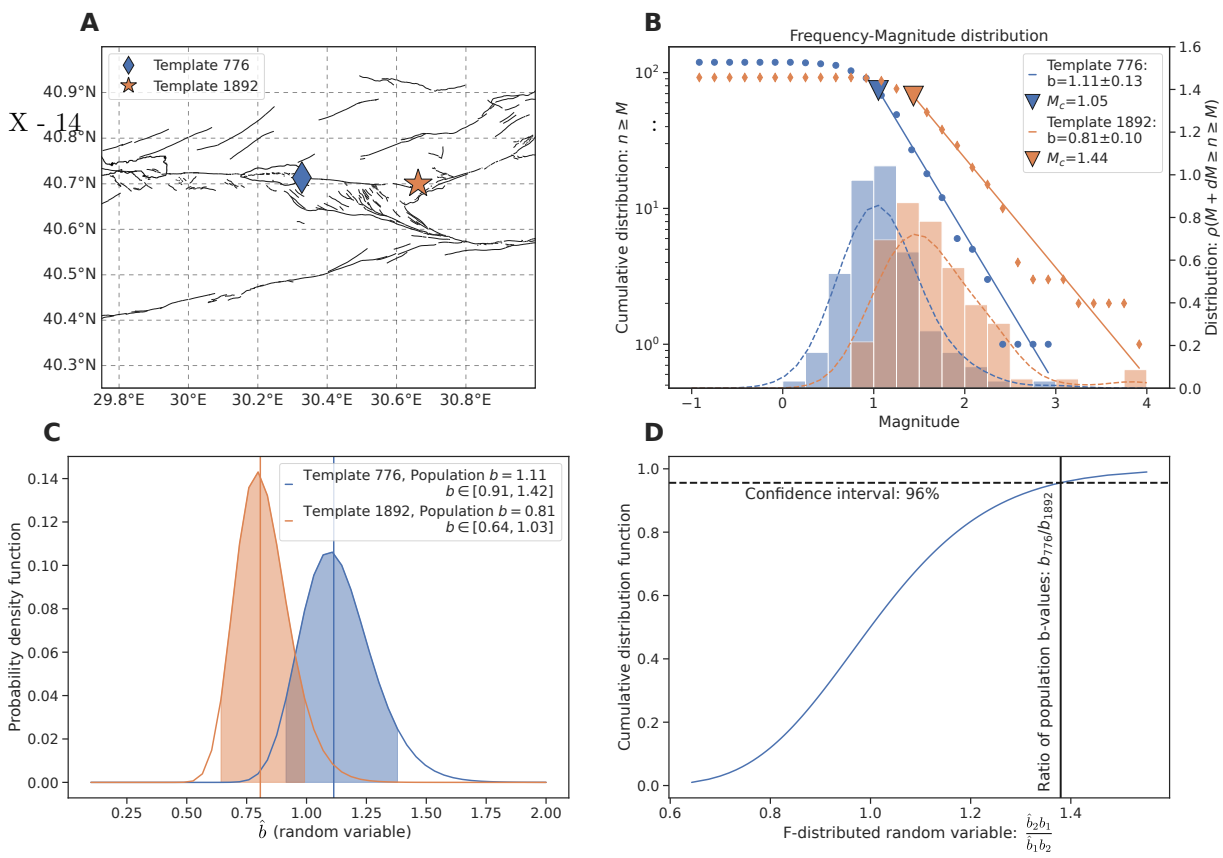


Figure S2. Estimation of the b-value and its uncertainties on two earthquake populations (two template families). **A:** Location of the two population centroids. Template 776 is located at the eastern side of Lake Sapanca and template 1892 is located near Akyazi. **B:** Cumulative (scatter plot) and non-cumulative (histogram) frequency-magnitude distributions. The dashed curves are the kernel density estimate of the non-cumulative probability density functions (pdf). The mode of the pdf is used as the magnitude of completeness (maximum curvature method). The b-value is computed with the maximum likelihood estimate (MLE, Equation (10)). **C:** The b-value pdf computed with Equation (11). The shaded area is the 90% confidence interval, also given in the legend. The b-value population is taken as the MLE (also shown with the vertical bars). **D:** Significance of the b-value difference between two populations using Equation (13). In this example, the b-value of template 776's event family is greater than template 1892's at the 96% confidence level.

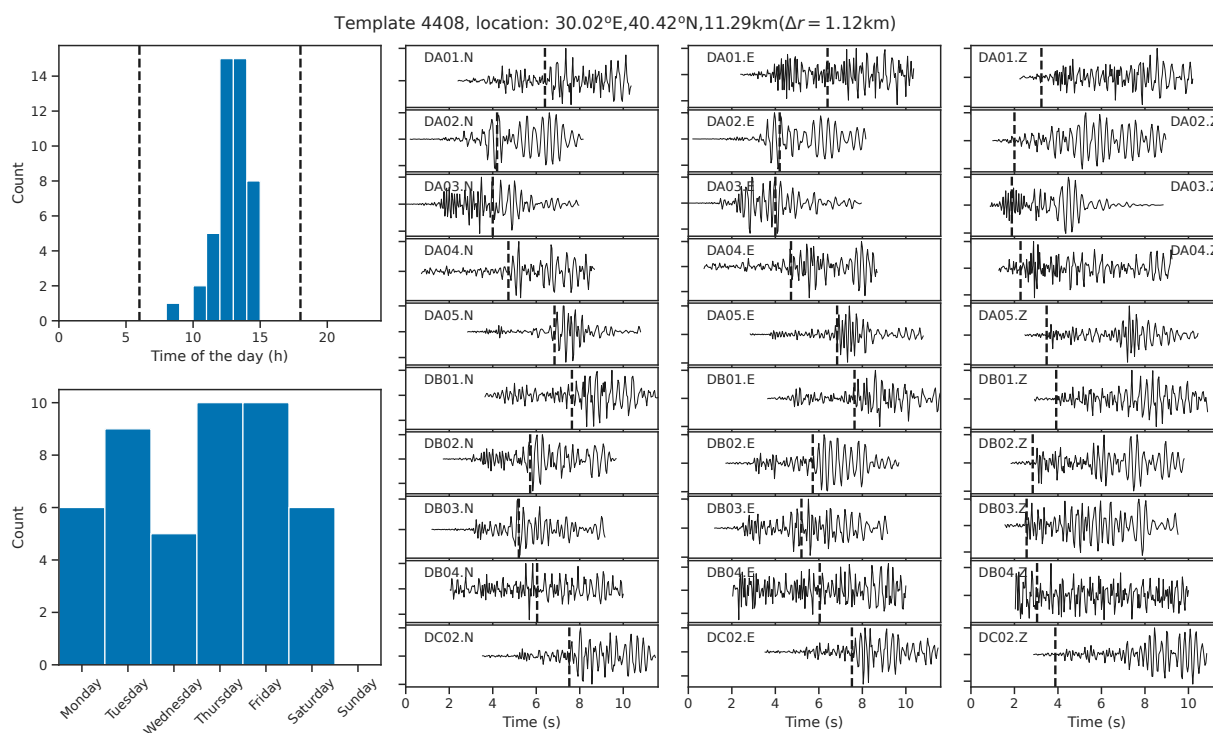


Figure S3. Top left panel: Mining-related seismicity is characterized by predominantly diurne seismicity, whereas we expect no preferred time for natural seismicity. In fact, natural seismicity shows slightly more events at night because noise is generally lower, and earthquake detection is easier. **Bottom left panel:** Mining-related seismicity also often shows no earthquakes on Sundays. **Right panels:** The waveforms produced by these mining-induced earthquakes have all characteristics of natural earthquakes, with clear P and S waves.

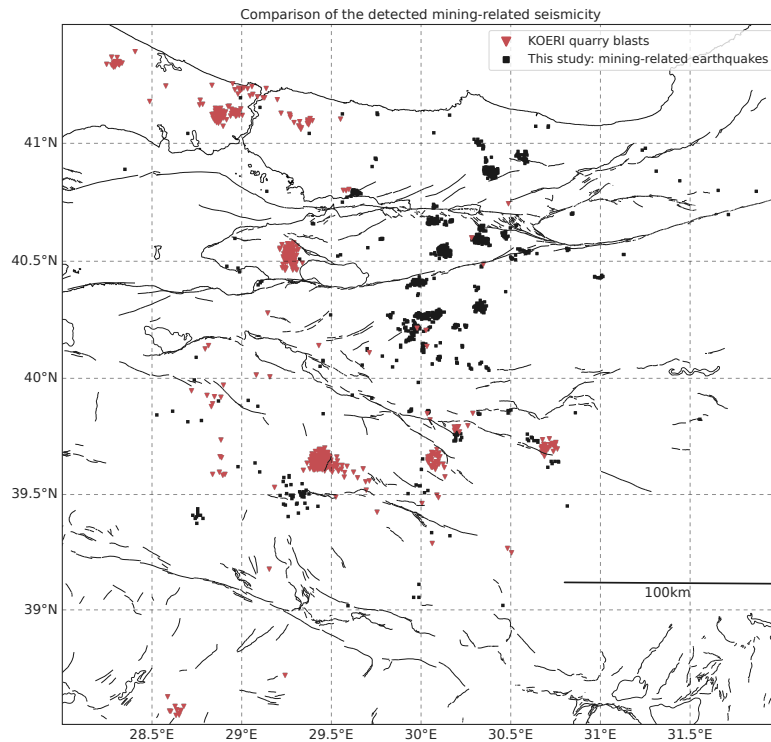


Figure S4. Comparison of the identified locations of mining-related seismicity in our catalog (black squares) with the reported explosions (red triangles) of the Kandilli catalog. Largest discrepancies appear beneath the DANA array. Discrepancies in the south are most likely due to the large location uncertainties ($h_{\max} > 10$ km) in our catalog.

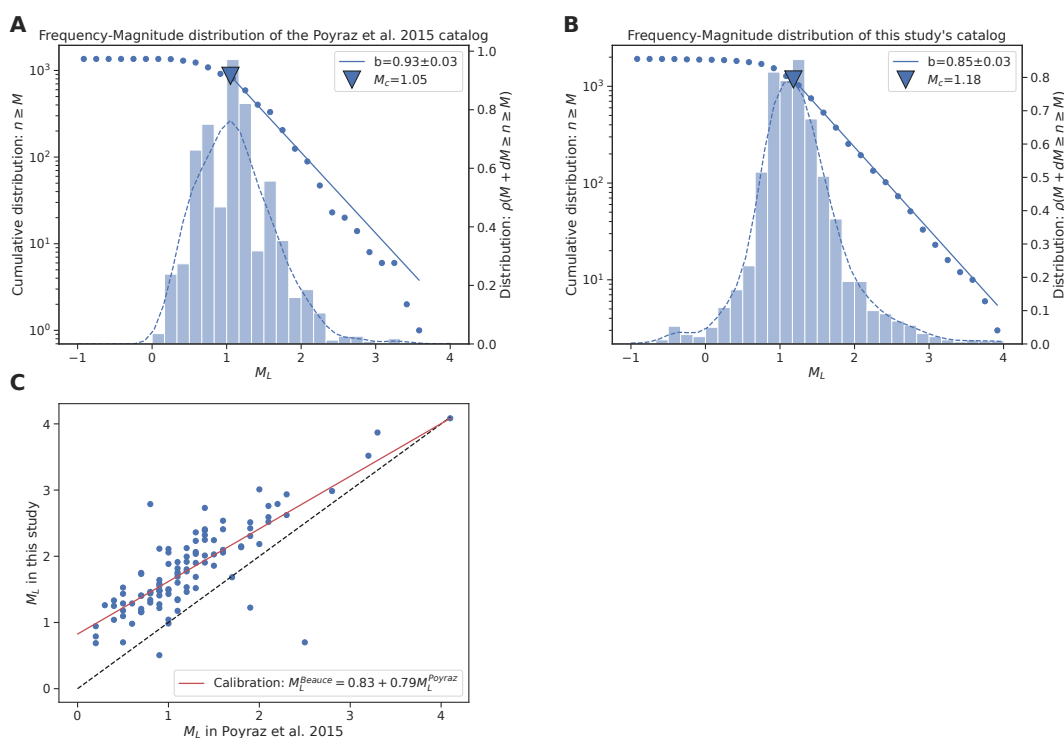


Figure S5. The b-value is computed with the maximum likelihood method (Aki, 1965). The magnitude of completeness M_c is computed with the maximum curvature method (Wiemer & Katsumata, 1999). **A:** Frequency-magnitude distribution of the catalog published in Poyraz et al. (2015). The total number of events is 1371. **B:** Frequency-magnitude distribution of this study's catalog without mining-related seismicity. The total number of natural earthquakes for which we could estimate a magnitude is 1929. Both b-values and magnitude of completeness are similar across catalogs. **C:** Comparison of the magnitudes computed in Poyraz et al. (2015) (x-axis) and in our study (y-axis) for events that were detected and characterized in both catalogs. Our magnitudes are larger for small events and the average magnitude difference is 0.57.

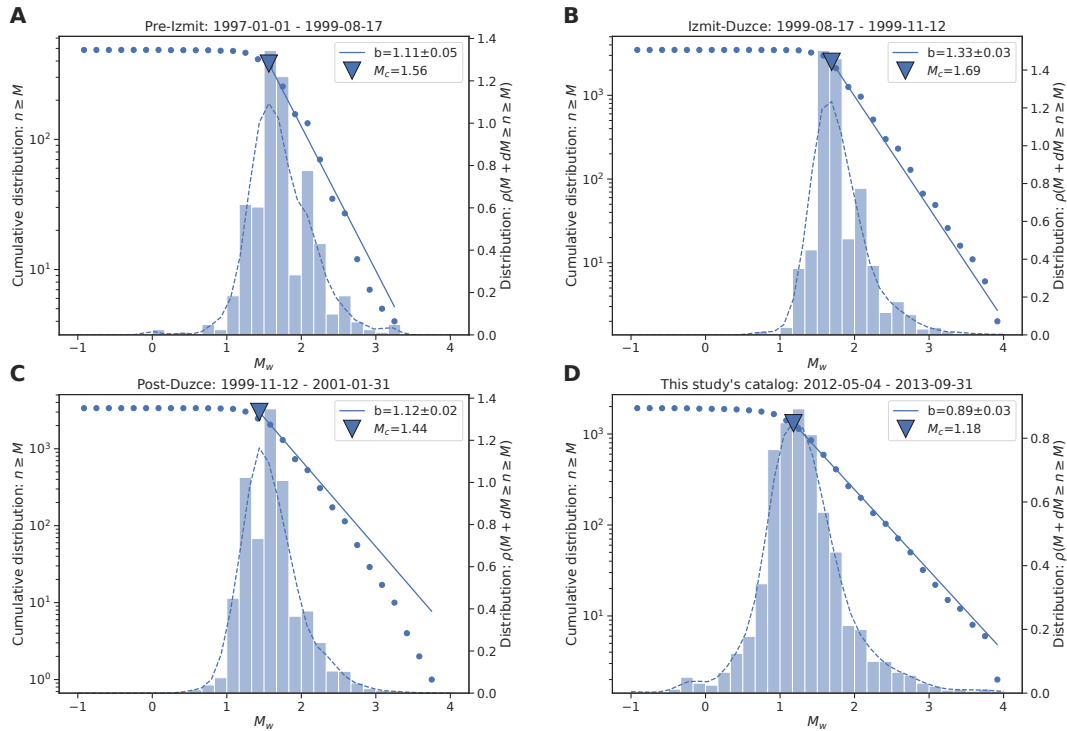


Figure S6. The b -value is computed with the maximum likelihood method (Aki, 1965). The magnitude of completeness M_c is computed with the maximum curvature method (Wiemer & Katsumata, 1999). **A:** Frequency-magnitude distribution of the pre-Izmit seismicity (Ickrath et al., 2015; Bohnhoff et al., 2016). **B:** Frequency-magnitude distribution of the Izmit-Düzce seismicity (Bulut et al., 2007; Bohnhoff et al., 2016). **C:** Frequency-Magnitude distribution of the post-Düzce seismicity (Ickrath et al., 2015). **D:** Frequency-Magnitude distribution of this study's catalog (without mining seismicity). We used our M_L - M_w calibration (see Figure S1B) to convert our local magnitudes to moment magnitudes.

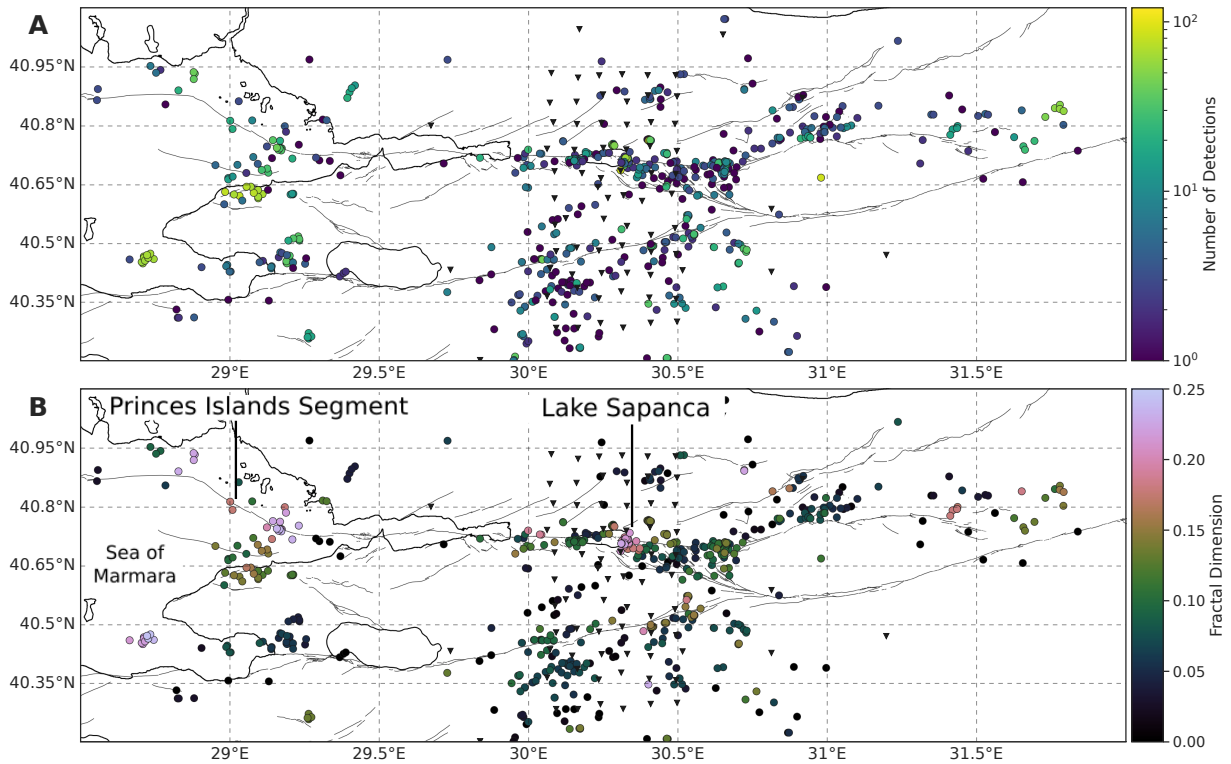


Figure S7. Earthquake clustering along the North Anatolian Fault Zone. **A:** Cumulative number of detections per template. **B:** Fractal dimension (as introduced in Figure 3 of the main manuscript). The eastern Sea of Marmara and Lake Sapanca show the strongest clustering along the NAF.

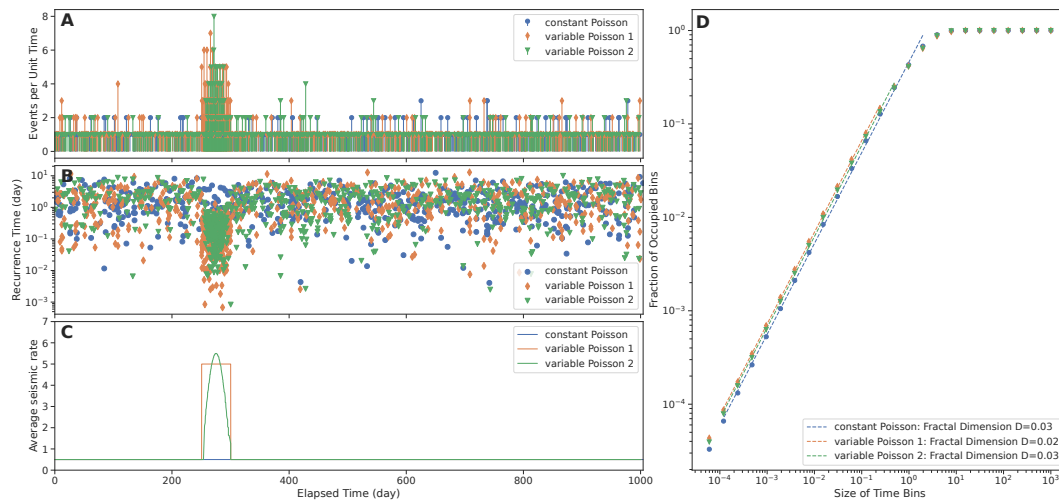


Figure S8. A Poisson point process cannot produce clustered seismicity, even with varying rate. **A:** Number of earthquakes per unit time. **B:** Recurrence time vs. origin time. **C:** Average number of earthquakes per unit time of the random Poisson process. **D:** Fractal analysis (see main manuscript) of the number of events per unit time. A transient increase in average seismicity rate does not reproduce a clustered seismicity with $D \neq 0$.